

Control of ionospheric plasma velocities by thermospheric winds

Thomas Immel (✉ immel@ssl.berkeley.edu)

University of California, Berkeley <https://orcid.org/0000-0003-2558-448X>

Brian Harding

University of California, Berkeley

Roderick Heelis

The University of Texas at Dallas

Astrid Maute

High Altitude Observatory <https://orcid.org/0000-0003-3393-0987>

JM Forbes

Univ Colorado

Scott England

Virginia Tech <https://orcid.org/0000-0001-5336-0040>

Stephen Mende

University of California, Berkeley

Christoph Englert

Naval Research Laboratory <https://orcid.org/0000-0002-2145-6168>

Russell Stoneback

University of Texas at Dallas

Kenneth Marr

Naval Research Laboratory

John Harlander

Space Systems Research Corporation

Jonathan Makela

University of Illinois

Article

Keywords: equatorial ionosphere, NASA Ionospheric Connection Explorer (ICON), thermospheric winds

Posted Date: January 16th, 2021

DOI: <https://doi.org/10.21203/rs.3.rs-131770/v1>

License:  This work is licensed under a Creative Commons Attribution 4.0 International License.

[Read Full License](#)

Version of Record: A version of this preprint was published at Nature Geoscience on November 29th, 2021. See the published version at <https://doi.org/10.1038/s41561-021-00848-4>.

Control of ionospheric plasma velocities by thermospheric winds

Thomas J. Immel^{1,9}, Brian J. Harding^{1,9}, Roderick A. Heelis², Astrid Maute³, Jeffrey M. Forbes⁴, Scott L. England⁵, Stephen B. Mende¹, Christoph R. Englert⁶, Russell A. Stoneback², Kenneth Marr⁶, John M. Harlander⁷, Jonathan J. Makela⁸

¹*Space Sciences Laboratory, University of California, Berkeley, CA*

²*University of Texas, Dallas, TX*

³*High Altitude Observatory, National Center for Atmospheric Research, Boulder, CO*

⁴*Department of Aerospace Engineering, University of Colorado, Boulder*

⁵*Virginia Polytechnic Institute and State University, Blacksburg, VA*

⁶*United States Naval Research Laboratory, Washington, DC*

⁷*Space Systems Research Corporation, Alexandria, VA*

⁸*University of Illinois, Urbana-Champaign, IL*

⁹*T.I. contributed equally to this work with B.H.*

Earth's equatorial ionosphere exhibits significant and unpredictable day-to-day variations in density and morphology¹⁻⁴. This presents difficulties in preparing for adverse impacts on technological systems even 24 hours in advance^{5,6}. This behavior is now theoretically understood as a manifestation of thermospheric weather, where conditions in the upper atmosphere respond strongly to changes in the spectrum of atmospheric waves that propagate into space from the lower and middle atmosphere, modifying the electrodynamic environ-

ment that exerts control over the creation of plasma⁷⁻¹⁰. The NASA Ionospheric Connection Explorer (ICON) makes the first coordinated space-based observations of the wind-driven dynamo and the plasma state to understand the relation of the plasma environment to the thermospheric weather below. Here we show the first direct measurements of the effects of a wind-driven dynamo in space, where a clear relationship is found between the vertical plasma velocities measured at the magnetic equator near 600 km and the thermospheric winds much farther below, with substantial correlations found between the plasma velocity and thermospheric winds during each of several successive precession cycles of the observatory's orbit. Prediction of thermospheric winds in the 100 – 150 km range emerges as a key to improved prediction of the Earth's plasma environment.

Accurate prediction of conditions in near-Earth space (from 100 to 1000 km altitude) is a goal that requires a capability to accurately simulate the nature of the interplay between the neutral gas and plasma environment around our planet. To achieve that goal, it is of critical importance to directly measure the response of the ionosphere to atmospheric forcing, both dynamical and chemical, to test and verify simulation developments and improve space weather predictions. The Ionospheric Connection Explorer (ICON¹¹) is a NASA mission launched in October 2019 to directly measure the process of ionospheric modification by the dynamics of the neutral atmosphere¹¹. The environment it observes exhibits a significant natural variability that is due in part to variation in the influences of the sun and its ionizing radiation, but clearly is also influenced by the lower and middle atmosphere which, during the first year of observations during solar minimum, are likely much more variable than solar sources. Understanding these influences and their impacts is a key

new area of research in space weather. This report describes the first evaluation of the electrodynamic impacts of the neutral wind environment on the ionosphere, with an investigation of the relation of the wind field to the motion of the plasma at the equator, where plasma densities are highest.

1 The Ionosphere

The highest density plasma in near-Earth space is a layer of O^+ ions surrounding the planet, usually with a peak density between 300 and 400 km altitude. Termed the F-layer, it is constituted of plasma produced by solar EUV radiation above 200 km. This source contributes to plasma densities at higher altitudes where recombination rates are much lower, creating a charged layer that persists into night. This layer of the ionosphere provides a conductive medium that has long been used to reflect radio and radar signals, but vertical and horizontal structuring of the layer can disperse these signals causing phase scintillation. High density also causes significant group delays in navigation systems. Because of its importance to these critical applications, the behavior of this layer has long been studied, and it has become clear that this layer often varies in ways that are impossible to relate to the dominant influences of solar radiation or periodic geomagnetic activity related to solar wind disturbances. The fact that the ionospheric plasma is weakly ionized, with at most 1% of the gas being ionized even at the F-peak, leads one to investigate the ways that interaction of the ionized species with the neutral atmosphere may produce ionospheric variability beyond that normally attributed to solar influences.

2 The Ionospheric Wind Dynamo

The daytime development of a persistent F-layer is, at high and middle latitudes, due largely to the balance of photochemical production and loss processes, where recently produced ions may easily diffuse to higher or lower altitudes along Earth's magnetic field. At the same time, the plasma in the ion-production region below 200 km (the E-region) strongly interacts with the parent neutral population. At lower latitudes, vertical diffusion is inhibited by the horizontal magnetic field, but a second mechanism can lead to even larger vertical ion transport: the equatorial wind dynamo. Solar heating puts the thermosphere into motion and the resultant thermospheric winds can generate electric currents in the dayside ionosphere that cause the plasma to drift perpendicular to the magnetic field. In general, this introduces vertical drift of the plasma at the equator in response to zonal horizontal winds¹². For this fact, and the strong insolation near the equator, the equatorial F-layer develops into the greatest reservoir of plasma on Earth. Modification of the thermospheric wind field in the daytime E-region can affect vertical drift of the plasma, and therefore the density of the F-layer produced. What is remarkable is the degree to which understanding of this process is based upon disparate, independent observations of plasma velocity, density, total electron content, and in rare cases, the wind in the E-region. Only recently have coordinated observations become available to allow complete investigations¹³. This report describes the first campaign of coordinated observations of the ionospheric wind dynamo and vertical plasma velocities in the equatorial ionosphere.

It has become clear that thermospheric winds can be affected by atmospheric wave phenom-

ena that originate in the neutral atmosphere below, down to the troposphere. This realization has developed over decades, beginning with the original concepts of lower atmospheric waves propagating into space in the 1960s. Hines¹⁴ was the first to derive the atmospheric wave equations that described propagation of energy and momentum in atmospheres via waves whose restoring force is gravity (non-acoustic). In considering these internal gravity waves as a source of ionospheric variability, Hines¹⁵ found that their greatest effects on the ionospheric plasma would be in modifying the electrodynamic environment, but argued that the effect would be minimal overall due to their small scale length. Following this work, the theory of larger scale atmospheric waves such as tides and planetary waves was developed^{16,17}, where the impact of tides on ionospheric conditions was evaluated and shown to explain the large scale ionospheric current systems derived from ground-based magnetometer measurements^{18,19}. However, the atmospheric tides considered in these studies were types driven directly by solar heating or lunar gravity, and as such exhibited no longitudinal structure and only slow daily variations. Only with new discoveries in the 21st century has the idea of tropospheric or stratospheric processes producing significant modifications of ionospheric density been considered plausible^{20,21}.

More recent investigations demonstrate that tides in the thermosphere may well originate from much lower altitudes and are of scales that could drive the larger scale electrodynamic of the system. Although a broad spectrum of waves are generated in the lower atmosphere, the most influential are those with long vertical wavelengths that span the dynamo region. One example is the diurnal, eastward-propagating, wavenumber-3 tide that is driven by cloud formation and solar IR absorption in the tropics, propagating upward to reach its highest amplitude (in horizontal wind

and temperature) well above 100 km^{2,22-24}. This tide varies throughout the year, and its amplitude and phase in the dynamo region can be evaluated by neutral wind and temperature measurements in the mesosphere and lower thermosphere²⁵. A corresponding variation in equatorial ionospheric drifts and densities, with a signature wave-4 structure (consistent with an asymptotic sampling of an eastward propagating wave-3 diurnal tide) has been observed with in-situ instrumentation²⁶, ultraviolet imaging²⁷ and radio occultation experiments²⁸ revealing a density variation that is much more highly structured than can be explained by solar radiation or solar wind forcing. A number of other tides propagate to and interact in this region, summarized in the review by England²⁹.

Efforts to simulate these effects and demonstrate the different interactions between the waves and the net effects on the ionosphere predict that lower atmospheric sources can introduce ionospheric variations on overall time scales of 10 days¹⁰ to as short as 24 hours⁷. Missing from this body of work is any direct investigation of how the dynamo wind modifications are actually transmitted to ionospheric altitudes, and what properties of the system may influence this connection. Our understanding of the space environment near Earth now relies completely on a new set of models that predict effects^{1,30-33} that have never been observed. Here we will show the degree to which variations in the atmosphere are manifested in the ionosphere via the dynamo mechanism.

3 Observations of dynamo wind effects

For the first time, ICON makes remote sensing measurements of the wind in the E-region region in conjunction with *in-situ* measurements of the plasma density and velocity in the F-region. This

is achieved through selection of an orbit and science payload that provide the coordinated measurements during each crossing of the magnetic equator³⁴⁻³⁶. The geometry of the observation is illustrated in Figure 1. For reference, the vertical (i.e., in the magnetic meridional plane) plasma velocity data from the in-situ Ion Velocity Meter (IVM) are shown at the locations of the observatory as sampled every 1 second, and the zonal wind profiles from the Michelson Interferometer for Global High-resolution Thermospheric Imaging (MIGHTI) are shown at their locations at the tangent point on the horizon. The wind measurements, retrieved in successive 30-s instrument integrations are available continuously from 100-300 km altitude in the daytime while plasma is being produced. As such, approximately half of all the 2700 orbits during the first six months of science operations provide these comparable measurements. In this illustration, only the zonal winds are shown; the meridional winds are also provided by MIGHTI. This analysis uses MIGHTI data from ICON Data Product 2.2 v03, and IVM data from ICON Data Product 2.7 v02. Meridional drift data from the IVM are preprocessed to ensure the 24h running median is zero, consistent with the expected nature of the quiet time ionosphere.

The physical process of generating an electromotive force with wind is understood in terms of Ohm's law applied in a weakly ionized atmosphere. Original work in this area was advanced in the 1960, culminating in work by Stening^{18,37}. Here the approach of Richmond³⁸ is followed, where the current is calculated in a non-orthogonal coordinate system defined by the magnetic field vector and the local horizon. Ohm's law is written:

$$\bar{j} = \underline{\sigma} \cdot (\bar{E} + \bar{u} \times \bar{B}) \quad (1)$$

where \bar{j} is the current density, \bar{E} is the electric field in a frame rotating with the Earth, \bar{u} is the neutral wind in the same frame, and \bar{B} is Earth's magnetic field. $\underline{\sigma}$ is the conductivity tensor.

In the daytime ionosphere, the conditions under which the ionosphere is produced, ICON can in principle provide each of the measurements that are needed to solve Ohm's Law for \bar{j} . ICON measures the velocity of the neutral gas directly. The velocity of the plasma measured at the observatory provides a direct measure of \bar{E} for the fact that the guiding center drift velocity of the plasma $\bar{v} = (\bar{E} \times \bar{B})/|\bar{B}|^2$, where \bar{B} is characterized by the International Geophysical Reference Field³⁹. The electric field \bar{E} can be determined from IVM plasma drift measurements and mapped along the magnetic field line that can be regarded as an equipotential, extending downward into the E-region. The conductivity terms are defined by the densities of the neutral gas and ionosphere, which compared to the remarkably structured neutral wind are generally in agreement with climatological reference models in the 100-150 km altitude range. To derive these, the International Reference Ionosphere⁴⁰ and the MSISE-00 reference atmosphere⁴¹ are used. In short, with ICON's measurements, one can directly calculate \bar{j} .

Although the neutral wind dynamo is a global system, the ionospheric drift can be approximated to be driven locally near noon, where horizontal conductivity gradients are lowest, and zonal gradients in the zonal current are small. The full derivation is shown in the Methods section but is briefly described here.

The local relationship is derived by calculating the terms of Ohm’s law and integrating the key quantities along the magnetic field line to predict the meridional plasma drift in the coordinate system described in Figure 2. This coordinate system is defined such that the zonal (x_1) and meridional (x_2) directions are both perpendicular to the local magnetic field (which is defined as the x_3 direction). The meridional direction (x_2) is defined to be positive downward at the magnetic apex, and the zonal direction (x_1) completes the coordinate system, generally horizontal eastward. For each MIGHTI wind measurement, the field-line integrated quantities of the Pedersen, Hall and Cowling conductivities (Σ_P , Σ_H , and Σ_C , respectively), and the conductivity-weighted zonal and meridional wind components ($U_1^{H,P}$ and $U_2^{H,P}$, respectively) are calculated. Requiring current continuity, a relationship is defined between the meridional drift at the apex of a magnetic field line and the wind drivers at the footpoint of that field line:

$$v_2 = - \left(\frac{\Sigma_H}{\Sigma_C} U_1^H + \frac{\Sigma_P}{\Sigma_C} U_2^P + \frac{\Sigma_H^2}{\Sigma_C \Sigma_P} U_2^H - \frac{\Sigma_H}{\Sigma_C} U_1^P \right) + C_{\text{ext}} \quad (2)$$

where the constant C_{ext} captures any offsets originating from non-local sources (as discussed in Section 4). This local relationship between meridional plasma velocity v_2 and conductivity-weighted horizontal neutral winds $U_{1,2}^{U,P}$ can be directly tested by ICON observations.

Our analysis focuses on periods where the precession of ICON’s orbit causes it to make repeated equatorial crossings near noon, where the height integrated wind-driven terms can be compared with the electric field measured at the magnetic apex. The ICON orbit crosses the equator at noon for several days a month, alternating between the ascending and descending node of the orbit. Once the orbit precesses to a noon-crossing configuration, ICON provides magnetically-connected wind and plasma drift measurements 11-12 times each day, performed over all geographic longi-

tudes except regions near South America where precipitating energetic particles disrupt the measurements and preclude the collection of valid wind data (the plasma drift measurements are unaffected). With these data, we can test our ability to use the wind observations to predict the plasma velocities.

For this test, we select three successive periods of noon-crossing observations from early in the ICON mission for analysis. Samples from the IVM and MIGHTI instrument are used when the local solar time is between 12h and 14h, and when the magnetic footpoint of ICON falls within 500 km of the MIGHTI wind data retrieved from the limb observations. This condition is met during about 4 minutes of each magnetic equatorial crossing. The average of the meridional drift of the plasma and the horizontal wind is determined in each crossing, and such observations are collected over 10 days to form a data set that extends in longitude around the planet. Figure 3 (top) compares the measured ion drift (v_2 in (2)) with the value predicted from the winds (right-hand side of (2)). Each marker represents one equatorial crossing. The Pearson correlation coefficient varies from 0.47 to 0.56 ($p < 0.01$, two-tailed t-test).

The population of equatorial crossings in the top panels comprises samples from many longitudes and several days. In order to isolate the longitudinal patterns (e.g., those arising from non-migrating tides), we next collect all noon-time data in these periods when the retrieved MIGHTI wind lies within 5° of 17° magnetic latitude and the IVM drift when ICON is within 5° of the magnetic equator. Data are subject to the same analysis used above, and collected into 24° bins of longitude (chosen because this is the amount of Earth rotation in one ICON orbit, and thus most

representative of ICON sampling).

The result is shown in Figure 3 (bottom). The green trace is the measured v_2 . The blue trace is the negative predicted v_2 , i.e., the term in parentheses in (2), or the total dynamo wind forcing term. For both traces, a constant zonal mean has been subtracted (the constant C_{ext} as discussed in the Methods section) to vary around a reference baseline of zero. If the dynamo were fully activated in the sense of zonal polarization current balancing wind-driven current perturbations, these two traces would be equal and opposite. In these data, opposing longitudinal patterns are seen.

It is informative to investigate the relative contribution of the specific wind-related terms in Equation 2 to the overall prediction of v_2 . Each of the four specific terms of the wind-driven dynamo calculation are shown for the last 10-day observation period in Figure 4. The black lines indicate terms associated with magnetic zonal winds, the grey lines with magnetic meridional winds. One finds that the zonal winds contribute to the largest variations of predicted meridional drifts, though the meridional winds provide significant inputs in some regions. Though the correlations with zonal wind drivers themselves are usually clear, the meridional wind is an important contributor in some cases. This provides support for a finding that the dynamo operates in a manner that is supported by theory, and that the derivation of its effects is correct in its inclusion of even minor terms that include the meridional wind.

4 Discussion

The results we report here represent the first direct measurement of the Earth’s equatorial wind dynamo, as winds just beyond the boundary of space drive changes in its plasma environment. It provides a necessary, and hitherto lacking, proof of the theoretical relationship between the circulation of gas in a magnetic planetary ionosphere and the electric fields generated by the transfer of its momentum to charged species. The results validate the steps taken in deriving the relationship between ICON’s plasma and wind measurements, described in detail in the Methods section.

The significant zonal gradients in Earth’s E-region winds observed at noon by the ICON observatory naturally lead to a prediction of strong variation in the magnetically-connected plasma drift. We find the measured plasma drifts at the magnetic equator respond accordingly, exhibiting a corresponding pattern of maxima and minima in locally averaged $v_2 \approx \pm 20$ m/s. These plasma velocity variations directly influence the abundance of plasma in the F-region²⁶. Though the zonal gradients in winds are likely attributable to lower atmospheric forcing of the winds in the lower thermosphere, the correlation coefficients reported in Figure 3 are derived with no specific knowledge of the tides or other forcing mechanisms responsible for the zonally varying pattern. For this study, the variations simply allow for the effect to be characterized in just a few days of noon-crossings.

The correlation shows the likely relation of the conductivity-weighted wind to the plasma drift on the same field line, with values consistently around 0.5 for each noon crossing. A portion of the statistical variance originates in the instantaneous uncertainties of the measured v_2 and $u_{1,2}$

when co-added in the ~ 4 -minute period of observations with each equator crossing, which are no more than ~ 3 m/s. These are notably low, and we find therefore that instrumental effects are likely not germane in the discussion of the spread of data around a linear relationship. There are other key areas to consider.

First, the potential lack of coherence of the wind field across the distance between the two footpoints of the field line, only one of which is observed, is likely a significant source of uncertainty. ICON is designed with an inherent ability to make wind observations at both footpoints about times per month and this capability is being exercised on orbit now to further investigate the potential effects of asymmetric forcing on meridional plasma drifts. Should the wind drivers at the unobserved conjugate footpoint differ from those observed to the north, then given the relationship revealed above, their inclusion would produce a likely-beneficial correction to the prediction of v_2 . Because these observations are localized in regions of high magnetic declination over the Pacific and Atlantic, a full daily-zonal characterization of drifts is not achievable and will require a different analysis.

Second, one must consider that the component of noon-sector plasma drift resulting from externally driven currents, as expressed by C_{ext} in Equation (20), may vary over the collection periods used in 3. This study shows that local forcing is specifically important in driving currents, but does not rule out sources of current outside of the observation window. With roughly 25% of the observed variation attributable to locally measured sources, a good portion of the variability remains to be attributed to other sources. Given the low solar activity, changes in E-region

conductivity across the dayside are minimal, and it is rather the thermospheric wind environment, driven by varying atmospheric tides from the troposphere, that may modify the electrodynamics on a global scale and introduce additional variability in the plasma drifts at noon.

Lastly, any small deviations from the approximation of $J_2 \approx 0$ would introduce variability in the plasma drift v_2 , not predicted by the wind observations. Future work combining the observations of ICON and orbiting magnetic observatories such as the ESA SWARM mission^{42,43} could provide further constraints on the sampling of wind first used here. Furthermore, such observations will allow the approach described here to be extended away from noon and toward the evening terminator, continuing to test our ability to predict the plasma velocity field.

The remarkable fact is that in each case reported here, the noon-time plasma drifts are always correlated with the wind drivers as they are repeatedly observed in magnetic conjunctions around the planet. This provides strong support for the recent, extensive effort in developing weather models to predict conditions in the middle and upper atmosphere, in simulations that assimilate measurements of tropospheric weather⁴⁴. It is clear that space weather cannot be predicted without good knowledge of tropospheric weather, and these models have been extended to altitudes above 100 km, where electrodynamic parameters including the full current equation are solved. The skill of these models in reproducing the MIGHTI-measured wind fields must be assessed, because in the case of success, it is then likely that they will also be able to provide the key to predicting the state of the ionosphere, as it changes remarkably from one day to the next.

Methods

Data for the Ionospheric Connection Explorer are available at <https://icon.ssl.berkeley.edu/Data>, and are to be permanently archived at NASA Space Physics Data Facility at <https://spdf.gsfc.nasa.gov>.

Derivation of wind vs. plasma drift

Neglecting currents from gravitational and pressure gradient forces, Ohm's law is written:

$$\bar{j} = \underline{\sigma} \cdot (\bar{E} + \bar{u} \times \bar{B}) \quad (3)$$

where \bar{j} is the current density, $\underline{\sigma}$ is the conductivity tensor, \bar{E} is the electric field in a frame rotating with the Earth, \bar{u} is the neutral wind in the same frame, and \bar{B} is the magnetic flux density. The conductivity tensor is defined in the ionosphere as

$$\underline{\sigma} = \begin{pmatrix} \sigma_P & \sigma_H & 0 \\ -\sigma_H & \sigma_P & 0 \\ 0 & 0 & \sigma_0 \end{pmatrix} \quad (4)$$

where σ_0 is the direct conductivity, σ_P is the Pedersen conductivity, and σ_H is the Hall conductivity.

On the time scales of several minutes, the observation period of each equatorial crossing, the electrostatic approximation holds. The divergence of Ampere's Law thus demands that currents are continuous:

$$\nabla \cdot \bar{j} = 0 \quad (5)$$

The coordinate system used here is shown in Figure 2, where “1” is perpendicular to \bar{B} , horizontal, and generally eastward, “2” is perpendicular to \bar{B} and generally downward, and “3” is in the direction of \bar{B} . Considering a magnetic field line with two “footpoints” in the lower atmosphere, and integrating this equation from the southern footpoint to the northern footpoint yields:

$$\int_S^N \nabla \cdot \bar{j} dx_3 = 0 \quad (6)$$

Integrating yields:

$$\frac{\partial J_1}{\partial x_1} + \frac{\partial J_2}{\partial x_2} + j_3^S - j_3^N = 0 \quad (7)$$

where the last two terms refer to currents in the insulating lower atmosphere, which are negligible, and J_1 and J_2 are field-line integrated currents:

$$J_1 = \int_S^N j_1 dx_3 \quad (8)$$

$$J_2 = \int_S^N j_2 dx_3 \quad (9)$$

$$(10)$$

Substituting into Ohm's law, J_1 and J_2 can be written:

$$J_1 = \Sigma_P(E_1 + U_2^P B) - \Sigma_H(E_2 - U_1^H B) \quad (11)$$

$$J_2 = \Sigma_P(E_2 - U_1^P B) + \Sigma_H(E_1 + U_2^H B) \quad (12)$$

where the U terms represent field-line integrated conductivity-weighted neutral winds, and Σ terms are field-line integrated conductances, shown below.

$$U_{(1,2)}^H = \frac{\int_S^N \sigma_H u_{(1,2)} dx_3}{\int_S^N \sigma_H dx_3} \quad (13)$$

$$U_{(1,2)}^P = \frac{\int_S^N \sigma_P u_{(1,2)} dx_3}{\int_S^N \sigma_P dx_3} \quad (14)$$

$$\Sigma_{H,P} = \int_S^N \sigma_{H,P} dx_3 \quad (15)$$

The integrals are performed assuming B and E are constant along the field line where the conductivity is significant. This assumption is supported in 3 ways: 1) Given the high conductivity parallel to B , it is clear that E can be presumed constant along the integration path, 2) Given that the major contributions to the integrated quantities comes from the dynamo regions, the relative variations B are minor, specifically in light of the fact that 3) the large variation in winds and conductivities along the field line are the major variables in the integral. When comparing drifts measured at the spacecraft to winds measured in the dynamo region, a correction of order $\sqrt{\frac{B_s}{B}}$ is needed, where B_s and B are the magnetic field at the spacecraft and in the dynamo region,

respectively. For ICON, which is at an altitude of 600 km, this correction is of order 10–20%. Neglecting this correction does not significantly affect the reported correlations in Section 3.

We now focus attention in the low latitude noon sector, where two simplifying approximations can be made:

1. Meridional currents are small and integrate to zero ($J_2 \approx 0$). The selection of noon near the equator places ICON's observations in a locale where the zonal current is the dominant component⁴⁵.
2. Zonal conductance gradients are small ($\frac{\partial \Sigma_P}{\partial x_1} \approx \frac{\partial \Sigma_H}{\partial x_1} \approx 0$). Near local noon the variation in solar illumination is small, and thus the variation in E-region plasma density is also small.

The first approximation yields $J_2 = 0$ in Equation 12; the relationship between the zonal and meridional electric field may then be written as

$$E_2 = -\frac{\Sigma_H}{\Sigma_P}(E_1 + U_2^H B) + U_1^P B \quad (16)$$

We consider the second approximation as it applies to Equation 7 which in the local noon sector reduces simply to:

$$\frac{\partial J_1}{\partial x_1} = 0. \quad (17)$$

Using Equations 11 and 16, we obtain the equation describing the action of the local dynamo near noon:

$$\Sigma_C \frac{\partial}{\partial x_1} E_1 + \frac{\partial}{\partial x_1} \left(\Sigma_H U_1^H + \Sigma_P U_2^P + \frac{\Sigma_H^2}{\Sigma_P} U_2^H - \Sigma_H U_1^P \right) B = 0 \quad (18)$$

where Σ_C is defined as a Cowling-like conductance:

$$\Sigma_C = \frac{\Sigma_H^2}{\Sigma_P} + \Sigma_P \quad (19)$$

Because we are interested in ionospheric motion, we rewrite Equation 18 in terms of $\bar{v} = \frac{-\bar{E} \times \bar{B}}{B^2}$ and rearrange terms:

$$\frac{\partial}{\partial x_1} v_2 = -\frac{\partial}{\partial x_1} \left(\frac{\Sigma_H}{\Sigma_C} U_1^H + \frac{\Sigma_P}{\Sigma_C} U_2^P + \frac{\Sigma_H^2}{\Sigma_C \Sigma_P} U_2^H - \frac{\Sigma_H}{\Sigma_C} U_1^P \right) \quad (20)$$

In derivative form, this equation represents the relationship between local variations observed in the winds and similar variations in the drift. Written in integrated form:

$$v_2 = - \left(\frac{\Sigma_H}{\Sigma_C} U_1^H + \frac{\Sigma_P}{\Sigma_C} U_2^P + \frac{\Sigma_H^2}{\Sigma_C \Sigma_P} U_2^H - \frac{\Sigma_H}{\Sigma_C} U_1^P \right) + C_{\text{ext}} \quad (21)$$

v_2 is now representative of the observed plasma drift, $U_1^{H,P}$ and $U_2^{H,P}$ are representative of the observed conductivity weighted winds, and a constant term is representative of an offset in the relationship between the winds and drifts that can be attributed to an external source of current. This is appropriate for ICON, for the fact that the derivative in the x_1 sense in either quantity is not exactly observed, except if considered between each of the noon-crossings that are separated by ~ 94 minutes. The value of the drift at the magnetic apex and the corresponding wind observation are observed directly by ICON. For comparisons of two crossings, it is necessary that the constant

offset not vary between the cases. Given the remarkably low solar activity and geomagnetic activity during the period of study, this is likely true over each individual period of noon crossings, which are separately studied in this report.

1. Liu, H. L. Variability and predictability of the space environment as related to lower atmosphere forcing. *Space Weather* **14**, 634–658 (2016).
2. Forbes, J. M., Palo, S. E. & Zhang, X. Variability of the ionosphere. *J. Geophys. Res.* **62**, 685–693 (2000).
3. Basu, S. *et al.* Day-to-day variability of the equatorial ionization anomaly and scintillations at dusk observed by GUVI and modeling by SAMI3. *J. Geophys. Res.* **114**, 1–12 (2009).
4. Villalobos, J. & Valladares, C. E. Statistical Analysis of TEC Distributions Observed Over South and Central America. *Radio Science* **55**, 1–20 (2020).
5. Eccles, J. V., St. Maurice, J. P. & Schunk, R. W. Mechanisms underlying the prereversal enhancement of the vertical plasma drift in the low-latitude ionosphere. *J. Geophys. Res.* **120**, 4950–4970 (2015).
6. Komjathy, A., Sparks, L., Mannucci, A. & Pi, X. An Assessment of the Current WAAS Ionospheric Correction Algorithm in the South American Region. *NAVIGATION* **50**, 193–204 (2003).
7. Liu, H.-L., Yudin, V. A. & Roble, R. G. Day-to-day ionospheric variability due to lower atmosphere perturbations. *Geophys. Res. Lett.* **40**, 665–670 (2013).

8. Fang, T. W., Fuller-Rowell, T., Yudin, V., Matsuo, T. & Viereck, R. Quantifying the Sources of Ionosphere Day-To-Day Variability. *Journal of Geophysical Research: Space Physics* **123**, 9682–9696 (2018).
9. Yamazaki, Y. *et al.* On the day-to-day variation of the equatorial electrojet during quiet periods. *J. Geophys. Res.* **119**, 6966–6980 (2014).
10. Pedatella, N. M. *et al.* Short-term nonmigrating tide variability in the mesosphere, thermosphere, and ionosphere. *J. Geophys. Res.* **121**, 3621–3633 (2016).
11. Immel, T. J. *et al.* The Ionospheric Connection Explorer Mission: Mission Goals and Design. *Space Sci. Rev.* **214**, 13 (2018).
12. Richmond, A. D., Matsushita, S. & Tarpley, J. D. On the production mechanism of electric currents and fields in the ionosphere. *J. Geophys. Res.* **81**, 547–555 (1976).
13. Pfaff, R. *et al.* Daytime dynamo electrodynamics with spiral currents driven by strong winds revealed by vapor trails and sounding rocket probes. *Geophys. Res. Lett.* **47**, e2020GL088803 (2020). E2020GL088803 2020GL088803.
14. Hines, C. O. Internal atmospheric gravity waves at ionospheric heights. *Can. Jou. Phys.* **38**, 1441–1481 (1960).
15. Hines, C. O. Wind-Induced Magnetic Fluctuations. *J. Geophys. Res.* **70**, 1758–1761 (1965).
16. Hines, C. O. Diurnal tide in the upper atmosphere. *J. Geophys. Res.* **71**, 1453–1459 (1966).

17. Forbes, J. M. & Lindzen, R. S. Atmospheric solar tides and their electrodynamic effects. I - The global Sq current system. II - The equatorial electrojet. *Journal of Atmospheric and Terrestrial Physics* **38**, 897–920 (1976).
18. Stenning, R. J. An assessment of the contributions of various tidal winds to the s_q current system. *Planet. Space Sci.* **17**, 889–908 (1969).
19. Tarpley, J. D. The ionospheric wind dynamo - I. Lunar tide. *Planet. Space Sci.* **18**, 1075–1090 (1970).
20. Millward, G. H. *et al.* An investigation into the influence of tidal forcing on F region equatorial vertical ion drift using a global ionosphere-thermosphere model with coupled electrodynamics. *J. Geophys. Res.* **106**, 24733–24744 (2001).
21. Immel, T. J. *et al.* The control of equatorial ionospheric morphology by atmospheric tides. *Geophys. Res. Lett.* **33**, L15108 (2006).
22. Hagan, M. E., Roble, R. G. & Hackney, J. Migrating thermospheric tides. *J. Geophys. Res.* **106**, 12739–12752 (2001).
23. Hagan, M. E. & Forbes, J. M. Migrating and nonmigrating diurnal tides in the middle and upper atmosphere excited by tropospheric latent heat release. *Journal of Geophysical Research (Atmospheres)* **107**, 6–1 (2002).
24. Zhang, X., Forbes, J. M. & Hagan, M. E. Longitudinal variation of tides in the mlt region: 2. relative effects of solar radiative and latent heating. *Journal of Geophysical Research: Space Physics* **115** (2010). URL

<https://agupubs.onlinelibrary.wiley.com/doi/abs/10.1029/2009JA014898>.

<https://agupubs.onlinelibrary.wiley.com/doi/pdf/10.1029/2009JA014898>.

25. Forbes, J. M. *et al.* Tidal variability in the ionospheric dynamo region. *J. Geophys. Res.* **113**, 2310–+ (2008).
 26. Kil, H. *et al.* Longitudinal structure of the vertical $E \times B$ drift and ion density seen from ROCSAT-1. *Geophys. Res. Lett.* **34**, 14110–+ (2007).
 27. England, S. L. *et al.* Effect of atmospheric tides on the morphology of the quiet time, postsunset equatorial ionospheric anomaly. *J. Geophys. Res.* **111**, A10S19 (2006).
 28. Lin, C. H. *et al.* Plausible effect of atmospheric tides on the equatorial ionosphere observed by the FORMOSAT-3/COSMIC: Three-dimensional electron density structures. *Geophys. Res. Lett.* **34**, 11112–+ (2007).
 29. England, S. L. A Review of the Effects of Non-migrating Atmospheric Tides on the Earth's Low-Latitude Ionosphere. *Space Sci. Rev.* **168**, 211–236 (2012).
 30. Jin, H., Miyoshi, Y., Fujiwara, H. & Shinagawa, H. Electrodynamics of the formation of ionospheric wave number 4 longitudinal structure. *J. Geophys. Res.* **113**, 9307 (2008).
 31. Wan, W. *et al.* A simulation study for the couplings between de3 tide and longitudinal wn4 structure in the thermosphere and ionosphere. *J. Atmos. Solar-Terr. Phys.* **90-91**, 52 – 60 (2012). URL <http://www.sciencedirect.com/science/article/pii/S136468261200123X>.
- Recent Progress in the Vertical Coupling in the Atmosphere-Ionosphere System.

32. Pedatella, N. M. & Liu, H. L. The Influence of Internal Atmospheric Variability on the Ionosphere Response to a Geomagnetic Storm. *Geophys. Res. Lett.* **45**, 4578–4585 (2018).
33. Liu, H.-L. Day-to-Day Variability of Prereversal Enhancement in the Vertical Ion Drift in Response to Large-Scale Forcing From the Lower Atmosphere. *Space Weather* **18**, e02334 (2020).
34. Englert, C. R. *et al.* Michelson Interferometer for Global High-Resolution Thermospheric Imaging (MIGHTI): Instrument Design and Calibration. *Space Sci. Rev.* (2017).
35. Harding, B. J. *et al.* The MIGHTI Wind Retrieval Algorithm: Description and Verification. *Space Sci. Rev.* **212**, 585–600 (2017).
36. Heelis, R. A. *et al.* Ion Velocity Measurements for the Ionospheric Connections Explorer. *Space Sci. Rev.* **212**, 615–629 (2017).
37. Stening, R. J. Calculation of electric currents in the ionosphere by an equivalent circuit method. *Planet. Space Sci.* **16**, 717–728 (1968).
38. Richmond, A. D. Ionospheric electrodynamics using magnetic apex coordinates. *J. Geomagn. Geoelectr.* **47**, 191–212 (1995).
39. Thébault, E. *et al.* Evaluation of candidate geomagnetic field models for IGRF-12. *Earth, Planets, and Space* **67**, 112 (2015).
40. Bilitza, D. IRI the International Standard for the Ionosphere. *Adv. Radio Sci.* **16**, 1–11 (2018).

41. Picone, J. M., Hedin, A. E., Drob, D. P. & Aikin, A. C. NRLMSISE-00 empirical model of the atmosphere: Statistical comparisons and scientific issues. *J. Geophys. Res.* **107**, 15–1 (2002).
42. Friis-Christensen, E., Lühr, H., Knudsen, D. & Haugmans, R. Swarm – an earth observation mission investigating geospace. *Adv. Space Res.* **41**, 210 – 216 (2008).
43. Lühr, H. *et al.* The interhemispheric and f region dynamo currents revisited with the Swarm constellation. *Geophys. Res. Lett.* **42**, 3069–3075 (2015).
44. Pedatella, N. M., Liu, H. L., Marsh, D. R., Raeder, K. & Anderson, J. L. Error growth in the Mesosphere and Lower Thermosphere Based on Hindcast Experiments in a Whole Atmosphere Model. *Space Weather* **17**, 1442–1460 (2019).
45. Pedatella, N. M., Forbes, J. M. & Richmond, A. D. Seasonal and longitudinal variations of the solar quiet (Sq) current system during solar minimum determined by CHAMP satellite magnetic field observations. *Journal of Geophysical Research (Space Physics)* **116**, A04317 (2011).

Acknowledgements We would like to thank the ICON engineering and operations teams for their outstanding performance during regional wildfires, power outages and a global pandemic to launch ICON and collect its data. ICON data are processed in the ICON data center at UC Berkeley and available through the internet (<https://icon.ssl.berkeley.edu>). All authors' effort are supported by NASA's Explorers Program through contracts NNG12FA45C and and NNG12FA42I.

Competing Interests The authors declare that they have no competing financial interests.

Correspondence Correspondence and requests for materials should be addressed to Thomas J. Immel (email: immel@ssl.berkeley.edu).

Figure 1 The design of the ICON mission provide simultaneous observations of the lower thermospheric dynamo winds and ionospheric plasma velocities when crossing Earth's magnetic equator. The diagram shows the location of the observatory ~ 590 km altitude, and a succession of magnetic field lines which uniquely connect the observatory to two remote locations at lower altitudes, north and south of the orbit track. In-situ ion drifts are made on field lines whose footpoints fall in the vicinity of the horizontal neutral wind vectors measured at the tangent point in the 100-200 km range. The sampling cadence of the plasma and wind velocities is 1s and 30s, respectively.

Figure 2 Diagram showing key properties of the equatorial ionosphere as it is influenced by the thermospheric wind dynamo. This coordinate system is defined such that the zonal (x_1) and meridional (x_2) directions are both perpendicular to the local magnetic field (which is defined as the x_3 direction). The meridional direction (x_2) is defined to be positive downward at the magnetic apex, and the zonal direction (x_1) completes the coordinate system, generally horizontal. For simplicity the zonal wind u_1 is shown, which by collisional drag may introduce motion of plasma perpendicular to the field line can drive zonal and upward currents j_1 and j_2 respectively. The redistribution of charge associated with these currents can introduce electric fields in each sense as well. Those electric fields introduce guiding center drift of the plasma perpendicular to the magnetic field, v_1 and v_2 . Vertical motion of the plasma perpendicular to the magnetic field is the most effective means of increasing plasma densities by lifting newly created plasma in the daytime to higher altitudes. The components of electric fields introduced by the localized redistribution of

charge due to winds are not separable from global scale effects, but are nonetheless present, with a varying SNR that ICON improves by making repeated measurements.

Figure 3 Predicted and observed meridional drift comparisons in three successive periods in early 2020. The three plots show the measured meridional drift v_2 and that predicted from wind driving parameters from (2) measured around the planet for 10-day periods starting on Feb. 3, Feb. 29 and March 22, 2020. Data are averaged between 12h and 14h local solar time. The plot scale is 15 m/s per radial step. Top panels show data from individual equator crossings, and bottom panels show longitudinally binned data. Pearson correlation coefficients are reported, and linear fits are shown. Error bars represent 1σ confidence in the mean value in each bin.

Figure 4 Plot showing different driving terms observed in 10-days of coordinated wind and plasma drift observations that provide zonal coverage and numerous samples for trend comparison. Error bars represent 1σ confidence in the mean value in each bin.

Figures

2020-01-15 01:46-01:56

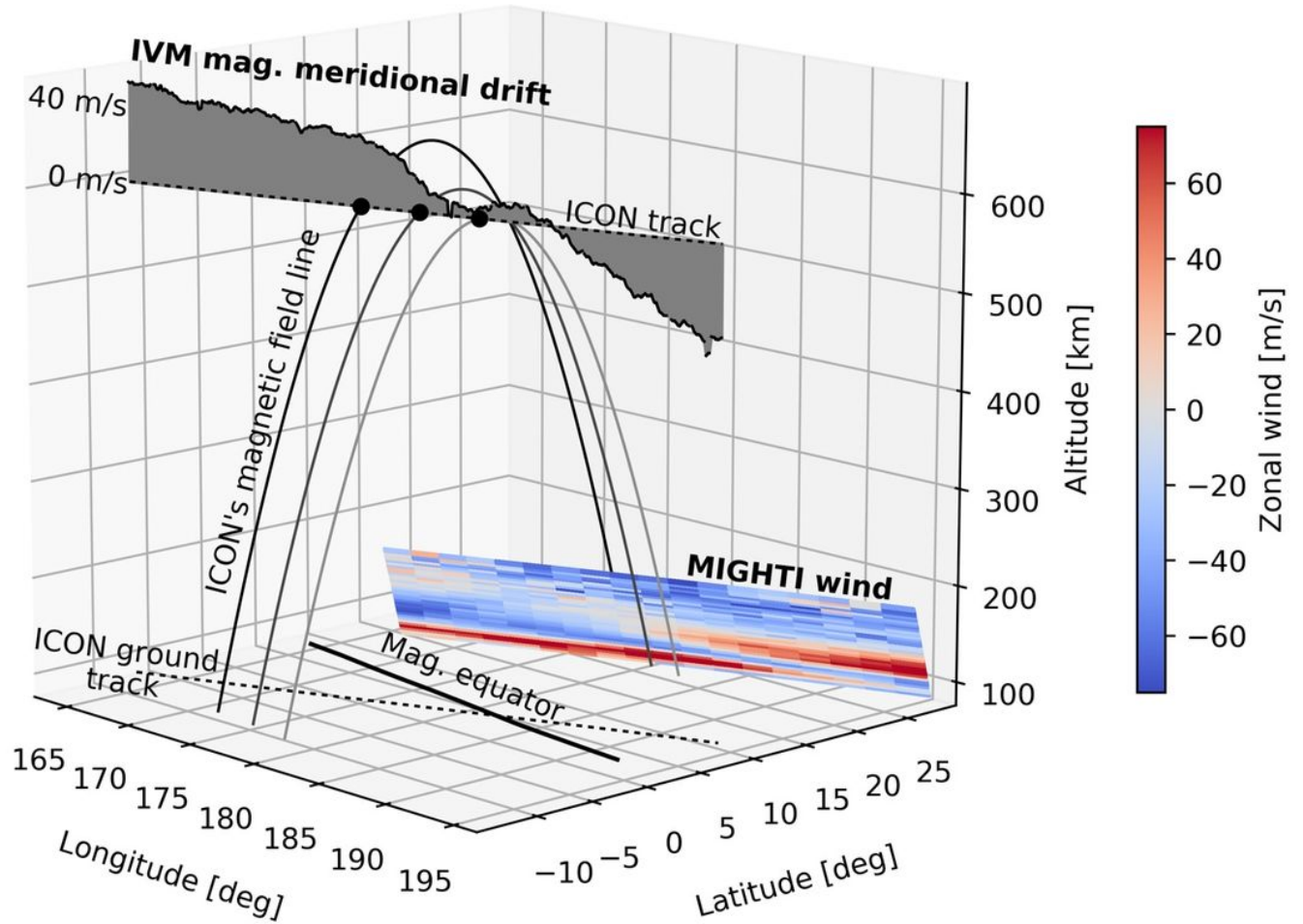


Figure 1

The design of the ICON mission provide simultaneous observations of the lower thermospheric dynamo winds and ionospheric plasma velocities when crossing Earth's magnetic equator. The diagram shows the location of the observatory ~590 km altitude, and a succession of magnetic field lines which uniquely connect the observatory to two remote locations at lower altitudes, north and south of the orbit track. In-situ ion drifts are made on field lines whose footpoints fall in the vicinity of the horizontal neutral wind vectors measured at the tangent point in the 100-200 km range. The sampling cadence of the plasma and wind velocities is 1s and 30s, respectively.

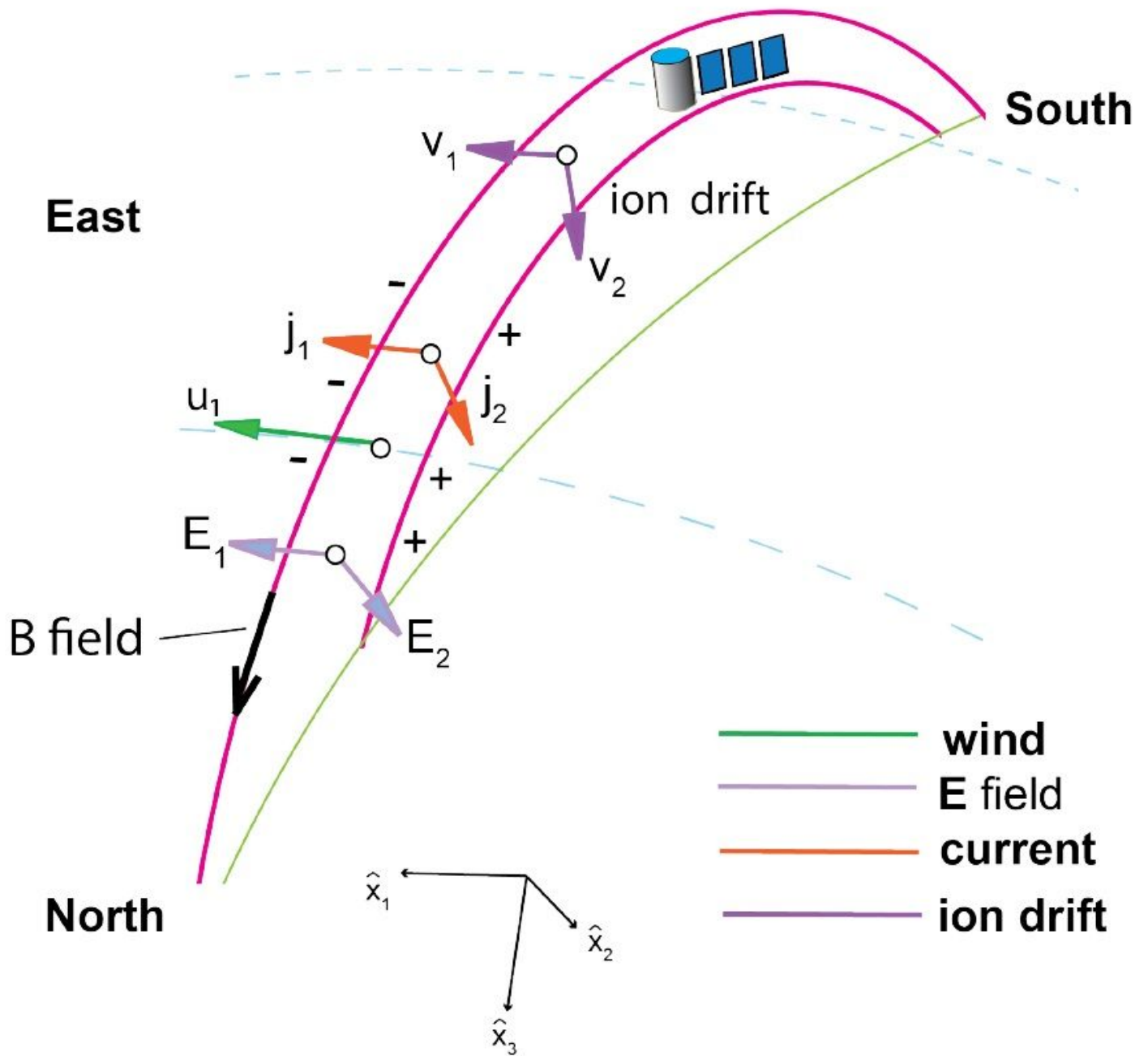


Figure 2

Diagram showing key properties of the equatorial ionosphere as it is influenced by the thermospheric wind dynamo. This coordinate system is defined such that the zonal (x_1) and meridional (x_2) directions are both perpendicular to the local magnetic field (which is defined as the x_3 direction). The meridional direction (x_2) is defined to be positive downward at the magnetic apex, and the zonal direction (x_1) completes the coordinate system, generally horizontal. For simplicity the zonal wind u_1 is shown, which by collisional drag may introduce motion of plasma perpendicular to the field line can drive zonal and upward currents j_1 and j_2 respectively. The redistribution of charge associated with these currents can introduce electric fields in each sense as well. Those electric fields introduce guiding center drift of the plasma perpendicular to the magnetic field, v_1 and v_2 . Vertical motion of the plasma perpendicular to

the magnetic field is the most effective means of increasing plasma densities by lifting newly created plasma in the daytime to higher altitudes. The components of electric fields introduced by the localized redistribution of charge due to winds are not separable from global scale effects, but are nonetheless present, with a varying SNR that ICON improves by making repeated measurements.

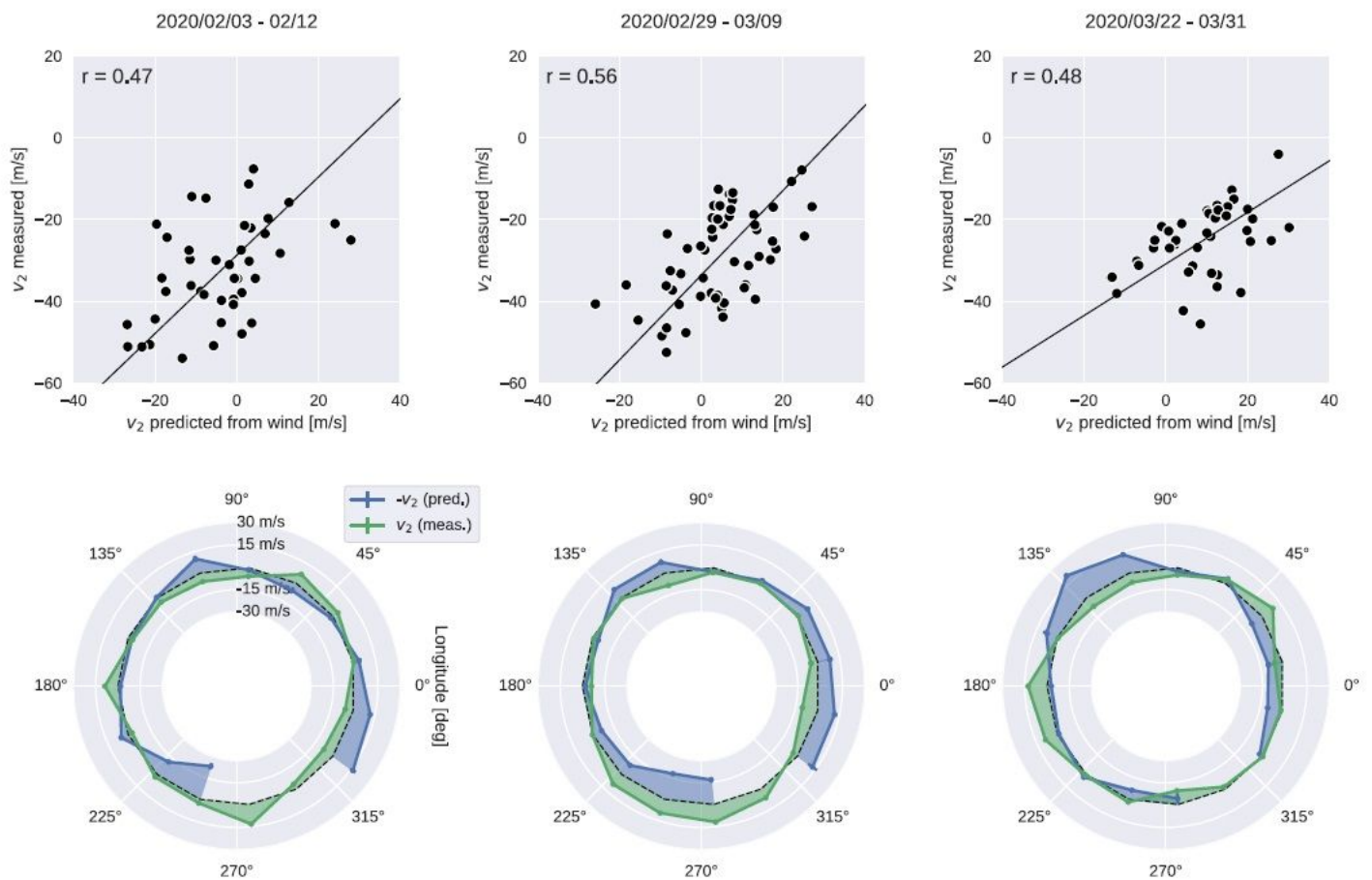


Figure 3

Predicted and observed meridional drift comparisons in three successive periods in early 2020. The three plots show the measured meridional drift v_2 and that predicted from wind driving parameters from (2) measured around the planet for 10-day periods starting on Feb. 3, Feb. 29 and March 22, 2020. Data are averaged between 12h and 14h local solar time. The plot scale is 15 m/s per radial step. Top panels show data from individual equator crossings, and bottom panels show longitudinally binned data. Pearson correlation coefficients are reported, and linear fits are shown. Error bars represent 1 σ confidence in the mean value in each bin.

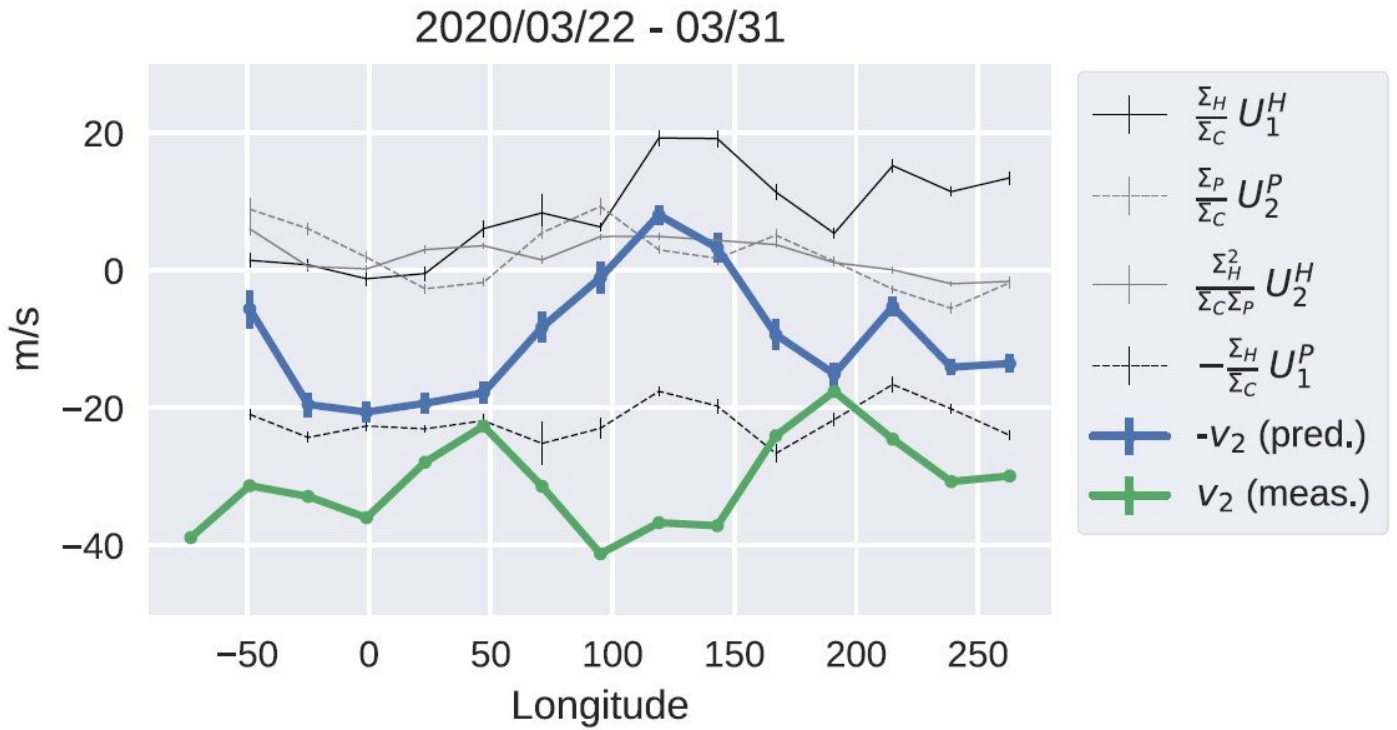


Figure 4

Plot showing different driving terms observed in 10-days of coordinated wind and plasma drift observations that provide zonal coverage and numerous samples for trend comparison. Error bars represent 1 σ confidence in the mean value in each bin.